




Computational proximity lithography with extreme ultraviolet radiation

VALERIE DEUTER,^{1,2,3,*} MACIEJ GROCHOWICZ,^{2,3,4,5} SASCHA BROSE,^{3,6} JAN BILLER,^{2,3,7} SERHIY DANYLYUK,⁸ THOMAS TAUBNER,⁴ AGNIESZKA SIEMION,⁵  DETLEV GRÜTZMACHER,^{1,3,7} AND LARISSA JUSCHKIN^{2,3,7}

¹Peter Grünberg Institute-10, Forschungszentrum Jülich, Wilhelm-Johnen Str. 1, 52425 Jülich, Germany

²Experimental Physics of EUV, RWTH Aachen University EUV, Steinbachstr. 15, 52074 Aachen, Germany

³JARA - Fundamentals of Future Information Technology, Wilhelm-Johnen Str. 1, 52425 Jülich, Germany

⁴Institute of Physics (IA), RWTH Aachen University, Otto-Blumenthal-Str., 52074 Aachen, Germany

⁵Faculty of Physics, WUT Warsaw University of Technology, Koszykowa 75, 00-662 Warsaw, Poland

⁶Chair for Technology of Optical Systems, RWTH Aachen University TOS, Steinbachstr. 15, 52074 Aachen, Germany

⁷Peter Grünberg Institute-9, Forschungszentrum Jülich, Wilhelm-Johnen Str. 1, 52425 Jülich, Germany

⁸Fraunhofer ILT - Institute for Laser Technology, Steinbachstr. 15, 52074 Aachen, Germany

*valerie.deuter@rwth-aachen.de

Abstract: The potential of extreme ultraviolet (EUV) computational proximity lithography for fabrication of arbitrary nanoscale patterns is investigated. We propose to use a holographic mask (attenuating phase shifting mask) consisting of structures of two phase levels. This approach allows printing of arbitrary, non-periodic structures without using high-resolution imaging optics. The holographic mask is designed for a wavelength of 13.5 nm with a conventional high-resolution electron beam resist as the phase shifting medium (pixel size 50 nm). The imaging performance is evaluated by using EUV radiation with different degrees of spatial coherence. Therefore exposures on identical masks are carried out with both undulator radiation at a synchrotron facility and plasma-based radiation at a laboratory setup.

Published by The Optical Society under the terms of the [Creative Commons Attribution 4.0 License](https://creativecommons.org/licenses/by/4.0/). Further distribution of this work must maintain attribution to the author(s) and the published article's title, journal citation, and DOI.

1. Introduction

While EUV lithography is gaining momentum in high-volume chip manufacturing, it may also be effectively used for custom nanopatterning utilizing especially diffraction and interference effects [1]. Substantial advantages of EUV lithography compared to other fabrication techniques, such as electron beam lithography, include minimal photoelectron blur, absence of charging effects and high throughput production due to the parallel patterning approach.

A special flavor of traditional lithography is proximity lithography, in which a mask is placed in the direct vicinity of a wafer, eliminating the optical system otherwise needed for the projection of the mask image onto the wafer. Proximity lithography may offer a low-cost alternative to the traditional imaging approach with potentially high throughput [2,3]. Decisive for image formation are diffraction effects, which occur at mask and during the propagation of light in the gap between mask and wafer. Utilizing these diffraction effects in the Fresnel regime, even complex geometries can be printed with proximity lithography [4]. In this regime, the mask transmission profiles are not exact replicas of the desired wafer prints. Instead, carefully designed mask features generate diffraction patterns at the wafer with finer details than that at the mask itself [5]. To obtain the desired intensity distribution at a chosen distance from the mask, computational proximity lithography is employed for the design of the mask features. The computational approach is

used for generating a synthetic holographic mask using a pattern at the wafer surface as input. With modern computational methods, the mask patterns can be generated even for non-periodic arbitrary wafer structures. This approach has been demonstrated for visible light [3,6]. In the present work, the application of the computational proximity lithography approach is explored for EUV radiation. In the sections below, we first address the design of the holographic mask using iterative algorithms for inverse propagation. Then, we discuss in detail the fabrication of the EUV phase-shifting mask. The exposures have been performed using a laboratory plasma-based EUV source as well as with synchrotron radiation. The comparison of the obtained patterns with the simulations is presented as well.

2. Holographic masks for computational proximity lithography

In this chapter, the iterative design process of holographic masks for computational proximity lithography and its limitations are described. Further on, a fabrication process of a specific holographic mask is presented.

2.1. Mask design for computational proximity lithography

In the EUV spectral range, most materials have significant differences in optical properties compared with the visible spectral range, which make the design of holographic mask more challenging. Here, the mask is designed by a numerical solution of the inverse problem starting from the desired intensity distribution at the wafer plane. At the mask plane, the light field distribution is computed using iterative wave propagation based on the Gerchberg-Saxton algorithm [7]. For the design of the holographic structure, the attenuation of EUV radiation within the mask material has to be considered. As the attenuation of EUV radiation is non-negligible for all materials, no purely phase-shifting masks can be achieved in this spectral range. The resulting mask is rather a so-called attenuating phase-shifting mask, where both phase and amplitude distributions are modulated. Such masks offer a higher diffraction efficiency in the EUV range than purely amplitude masks [1,8,9]. The mask, or hologram, is computed using an algorithm that requires the iterative light field propagation between mask (object) and wafer (image) planes. The goal is to find a phase distribution at the mask plane, which generates after propagation the desired intensity distribution in the wafer plane. In addition to numerical constraints, also manufacturing capabilities have to be taken into account, including the size of the smallest manufacturable element and the topography of the mask: by varying the thickness of the phase shifting material different phase shifts are obtained. By modulating the material thickness of each pixel (thickness up to 330 nm, lateral size 50 nm x 50 nm), also the intensity is changed due to very high attenuation of EUV radiation. The developed algorithm consists of the following steps (see Fig. 1):

1. The algorithm starts at the wafer plane with a wavefront constructed from the desired intensity distribution $I_0 = I_{target}$ and a random distribution of the phase.
2. Subsequently, this wavefront is (back-)propagated to the mask plane using the angular spectrum of plane waves method (ASPW). Thus, the intensity and the phase of the wavefront at the mask plane are computed. In the original Gerchberg-Saxton (GS) algorithm, the intensity would be updated at this stage to the source intensity (uniform distribution in our case) and the phase kept untouched. However, due to our manufacturing capabilities and the high attenuation of EUV light in the mask material, the algorithm needs to be modified: for each pixel, the obtained phase value is changed to the nearest available discrete phase level. Then, the intensity is updated to show the effect of attenuation of EUV radiation in the material.
3. The updated wavefront is propagated forward to the wafer plane.

4. At the wafer plane, the intensity distribution is translated in a resist profile based on the exposure model [10] and resist contrast parameters. The resist response function (see sub-chapter constrains) is used to simulate the remaining resist thickness. For the obtained profile, the following three evaluation metrics are applied: l2-norm, signal to noise ratio (SNR) and normalized image log slope (NILS). The l2-norm was used in the original GS algorithm and is minimized [7]. The SNR is defined as the ratio of light intensity in the signal window (desired pattern) to the intensity in areas outside the desired pattern. NILS is a metric extensively used in lithography to assess the quality of aerial image and resulting patterns [10]. This metric gives information on the edge sharpness an intensity distribution. Both SNR and NILS are maximized. Then the obtained intensity is updated to the target distribution $I = I_{target}$ while the phase distribution remains unchanged $\varphi_{i+1} = \varphi$.
5. Using the result as input, the next iteration starts.

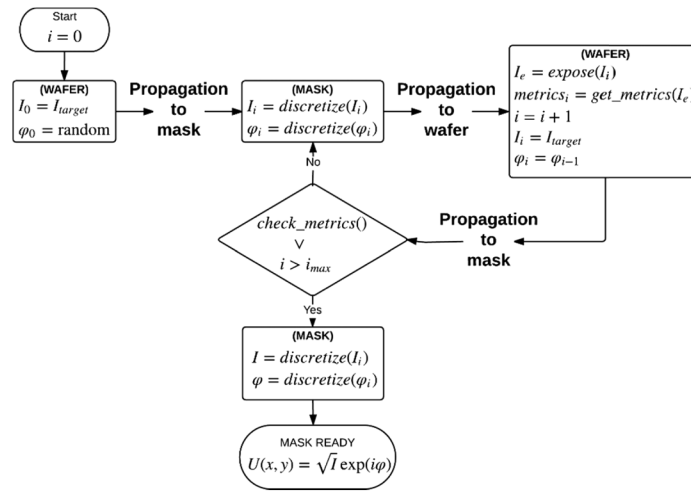


Fig. 1. Algorithm flow for the design process of the synthetic holographic mask.

This algorithm loop is interrupted when either an acceptable tolerance on the difference between the resist profile obtained from the exposure model and the desired normalized exposure profile or the maximum number of iterations is reached. Upon termination, the phase and the intensity values are discretized for the last time. This results in the final phase and intensity distributions, which are transformed into a topographic holographic mask design. In this design, the material thickness of each pixel (e.g. no material or 330 nm material in the case when only two discrete phase levels are selected) corresponds to both phase and intensity modulations.

2.2. Constrains

To adapt the algorithm to the experimental conditions, the following measures are implemented: the phase/intensity profile at the mask is not continuous, but consists of a limited number of phase/intensity levels selectable by a designer and limited by the fabrication process; the minimal element size on the mask (pixel size) is restricted to the manufacturing capabilities; the correlation between absorption and phase-shifting properties of the mask material is accounted for in the computations; the resist response function is applied prior to the evaluation of the obtained exposure results. The resist response function, defined as a dependence of normalized resist thickness on the exposure dose, is approximated by a piecewise linear curve [11]. Three main regions may be distinguished: fully exposed (with dose D higher the dose to clear D_h ,

$D > D_h$), not exposed at all (dose smaller than onset dose D_1 , $D < D_1$) and an intermediate level ($D_1 \leq D \leq D_h$). Areas of fully exposed and not exposed at all define the resulting lateral geometry of the exposed resist structure. The resist contrast is calculated using the following equation: $\log_{10}(D_h/D_1)^{-1}$ [8,9,12,13].

For the present feasibility study, we use elbow test structures with different dimensions as target resist structures in wafer plane. The design process of the holographic mask layout is computed as described above for the illumination wavelength of 13.5 nm. Furthermore, the number of phase levels for the mask is limited to only two levels (full resist thickness and no resist on mask) to alleviate the fabrication process. With the limitation of the fabrication process, a pixel size of $50 \times 50 \text{ nm}^2$ is feasible. Figure 2 shows one of the 16 different elbow test structures Fig. 2 (b) with its corresponding mask counterpart Fig. 2 (a). The elbow structures differ in feature width (from 100 nm to 800 nm) and pitch size (from 200 nm to 1600 nm) and are realized as individual test structures on the holographic mask.

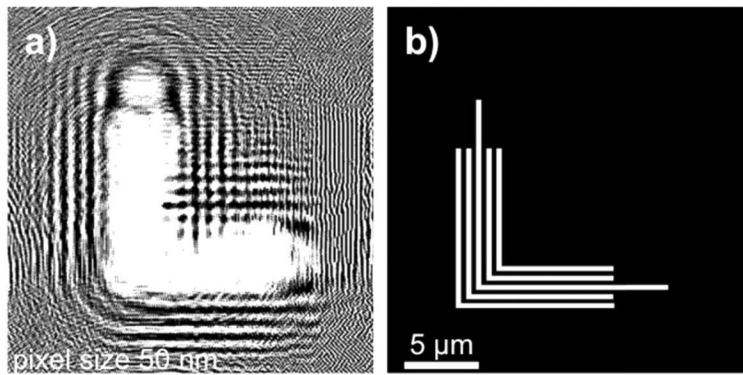


Fig. 2. The elbow test structure in wafer plane consists of line structures with a feature width of 350 nm and a periodicity of 700 nm (b) and the corresponding mask design (pixel size $50 \times 50 \text{ nm}^2$) (a). (a) Resist-covered pixels are shown in black, openings in white, (b) fully exposed resist corresponds to white, non-exposed to black for the positive tone EUV resist (inverted for negative tone resist).

The hologram is designed for a monochromatic wavelength of 13.5 nm, however its performance is verified for partial coherence illumination and the spectral properties of the illumination (bandwidth $\Delta\lambda/\lambda = 4\%$, spatial coherence length $l_{\text{plasma}} = 13.5 \text{ μm}$ and $l_{\text{synchrotron}} = 1.19 \text{ mm}$ [10,11]).

Figure 3 shows the simulated exposure result of one elbow structure illuminated with temporally coherent (a) and incoherent (c) illumination in focus position for the same mask and the intensity distribution along the red cutline (b and d) [8]. The red cutline represents an average over ten rows of pixels. Figure 4 shows of those intensity cutline distributions for exposure results distant within $\pm 500 \text{ nm}$ around the focal distance both for coherent and incoherent illumination. The contrast near the focal point is higher for coherent illumination, however the depth of focus increases for the incoherent case.

A mask-wafer distance of $e = 300 \text{ μm}$ is chosen due to the fact that it allows for reliable positioning of the individual components in the utilized experimental setups. The depth of focus (DOF) is defined as a distance range with critical dimension's deviation from the target smaller than 16% (two-pixel deviation). The determined DOF for incoherent illumination is equal to 725 nm. Taking the small DOF into consideration, a mask-wafer distance scan has to be performed.

2.3. Mask fabrication and characterization

As phase shifting material for the holographic mask, the positive tone electron beam resist CSAR 62 [14] is used, due to its optimal optical properties at 13.5 nm wavelength (acceptable absorption

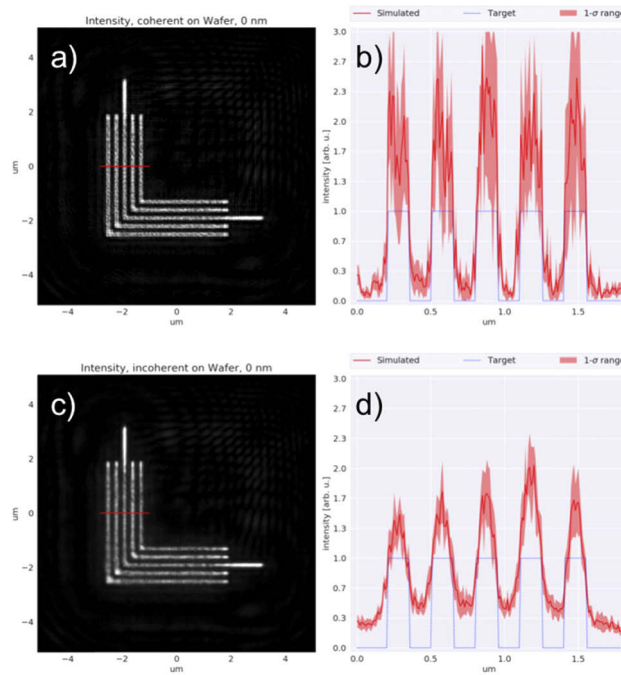


Fig. 3. The intensity distribution at focal point for temporally coherent (a) and incoherent illumination (c) and the corresponding cross-sections across the intensity pattern in the mask plane (b) and (d).

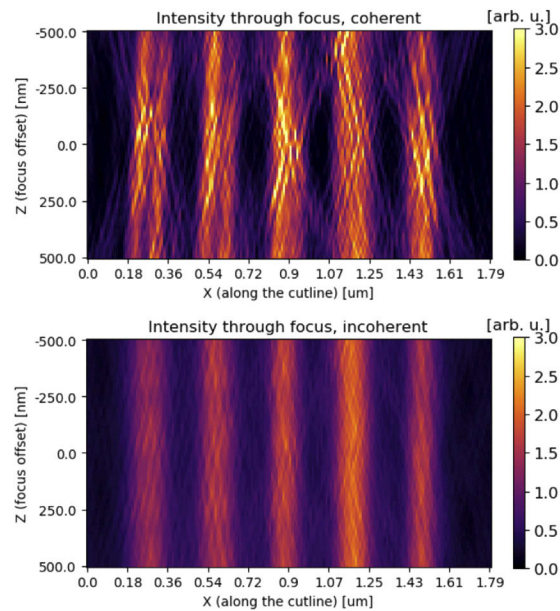


Fig. 4. The red cutline (Figs. 3 (a) and (c)) intensity distribution along the propagation axis for coherent (top) and incoherent (bottom) illumination.

$A_{\text{CSAR}, 330 \text{ nm}} = 66.56\%$ [15] with sufficient phase shift $\Phi_{\text{CSAR}, 330 \text{ nm}} = 0.88 \pi$ [16,17]). With respect to mask lifetime, using the resist as a phase-shifting material for EUV wavelengths is enabled by the relatively low available intensities in the laboratory setup ($< 1 \text{ mW/cm}^2$). No pattern degradation has been observed for total exposure doses up to 2 J/cm^2 for a resist with similar chemical composition used as mask phase-shifting material [18]. Here, the holographic mask structure is fabricated on a 30 nm silicon nitride (SiN) membrane by a simple four-step fabrication process without requiring a structure transfer step. As this fabrication process has been reported before [18,19], it will be explained here only shortly, see Fig. 5. First, the membrane is spin-coated with CSAR 62 resist of 330 nm thickness using hexamethyldisilazane (HMDS) as an adhesion layer. Second, the holographic structures are written in the resist using electron beam lithography (EBL, dose = $350 \mu\text{C}$, 100 keV acceleration voltage). Third, the structures are developed in AR600-546 [14] at 0°C for 90 s. Two subsequent isopropanol baths at room temperature for 30 s each stop the development. Fourth, the mask is hard baked for 60 s at 130°C to improve its stability under EUV illumination [19].

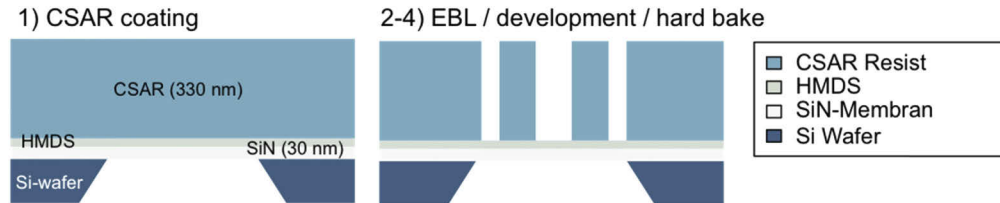


Fig. 5. The process flow of the holographic mask fabrication (EBL = electron beam lithography).

As discussed in the previous section, the holographic mask is designed for two phase levels, the mask-wafer gap is selected to $300 \mu\text{m}$ and the mask pixel size is set to $50 \times 50 \text{ nm}^2$.

Figure 6 shows an atomic force microscopy (AFM) scan Fig. 6(b) and a scanning electron microscopy (SEM) image Fig. 6(c) of one of the elbow-counterpart structures of the fabricated mask in comparison to the calculated design Fig. 6(a). Figures 6(d) and (e) show a comparison between the zoomed-in inner structures of the calculated and fabricated design respectively. For a better contrast of the CSAR 62 resist during SEM imaging, the mask was covered with 3 nm layer of iridium. By comparing the simulated and the fabricated structures some deviations occur, especially the resist islands of only a few pixels do not appear in the structures after the development process.

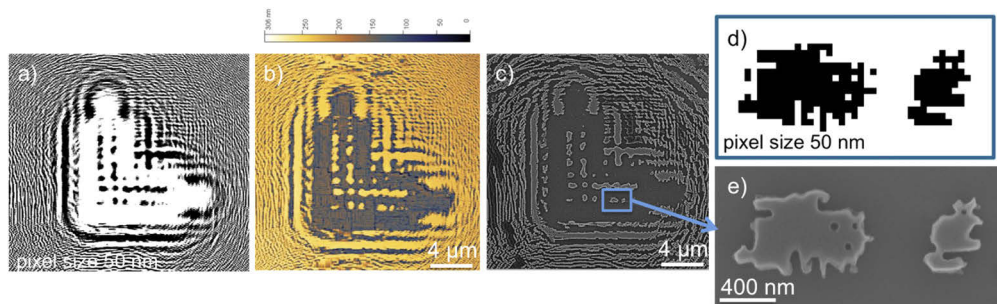


Fig. 6. The simulated mask geometry (a) with a close-up (d) in comparison to the fabricated mask geometry: inspected by means of AFM (b) and SEM (c, e). The resist is represented in black in a) and d) and appears brighter in b), c) and e).

To investigate the obtained thickness profile of structured CSAR 62 resist on the mask, cross-sections of the mask were obtained after EUV exposures by means of focused ion beam processing, see Fig. 7. Even though the resist is spin-coated on the membrane with the desired thickness of 375.4 ± 6.9 nm as confirmed by spectral ellipsometry measurement, the cross-sections reveal that the height of the phase shifting structures is much smaller (74.1 nm) and exhibits substantial variations of ± 48.9 nm (see Fig. 7). The membrane is covered with a solid CSAR 62 under-layer from which the phase shifting structures of different height raise. The fabricated mask has therefore more than two phase levels with a much smaller phase shift than initially designed.

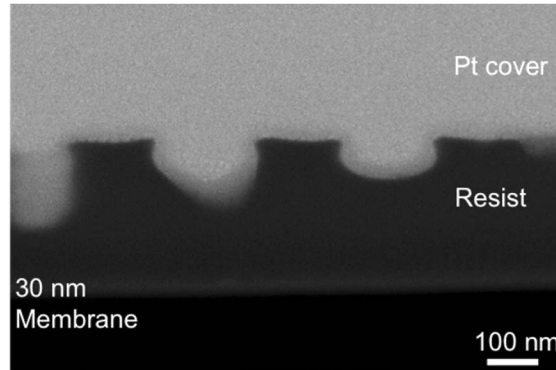


Fig. 7. FIB-cut of a holographic mask (side profile).

Consequently, the electron beam writing process and the development step did not result in developing the CSAR 62 resist all the way through. This is due to a challenging aspect ratio of 6.6 and therefore the developer likely did not reach all areas properly in the same way. This can be improved in the future by using a mega-sonic bath during the development process and further adjustment of the parameters of the electron beam writing. However, CSAR 62 resist is a suitable phase shifting material as its optical constants are as expected. The measured transmission of a membrane with spin-coated resist of 380 nm thickness amounts to $T_{total} = 22.5\%$ with $T_{CSAR} = 27.5\%$ and $T_{membrane} = 81.7\%$ [19], which is in line with the model data from CXRO [15].

3. EUV exposures

For the evaluation of computational proximity lithography, the obtained holographic masks have been exposed to radiation of a wavelength of 13.5 nm provided by a plasma-based source (spatial coherence length 13.5 μm) [20] and a synchrotron source at Paul Scherrer Institute PSI (spatial coherence length 1.19 mm) [21]. For the exposures with the laboratory exposure tool, a positive tone EUV chemically amplified resist (CAR) is used. CAR offers sufficient sensitivity and contrast of 14.9 for the limited available intensity in the wafer plane of $I_{plasma} = 0.04$ mW/cm² when operated at 13.5 nm wavelength [20]. At the synchrotron facility, a negative tone resist based on a hydrogen silsesquioxane (HSQ) platform is used. HSQ offers a comparable high resist contrast as CAR but at lower sensitivity [22], which is acceptable due to the available intensity of $I_{synchrotron} = 5.93$ mW/cm² [21].

Due to the small depth of focus of ~ 725 nm for the designed holographic mask, a mask-wafer distance scan has been performed to determine the effective “focal distance” of the holographic mask. The designed focal distance is 300 μm . First, the exposures with plasma-based radiation and second, the exposure results with synchrotron radiation are described. The images in Fig. 8 show the resulting prints in resist on the exposed wafers in dependence of the distance between mask and wafer for plasma-based radiation.

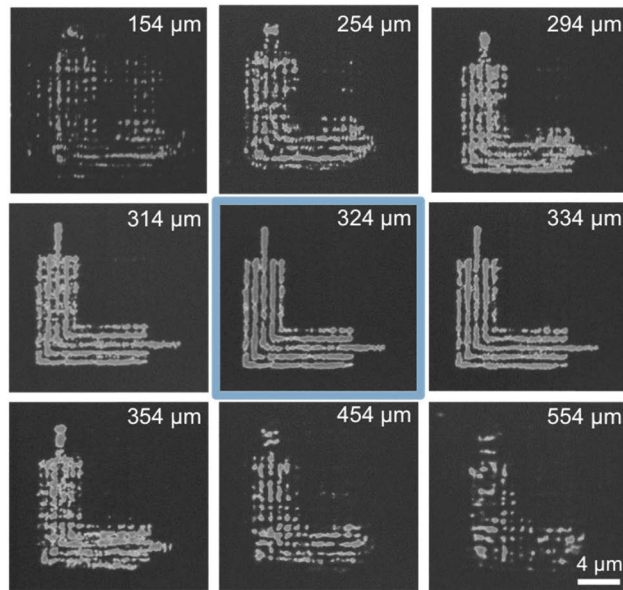


Fig. 8. The exposure results for the mask-wafer distance scan of one elbow structure with plasma-based source ($\lambda = 13.5$ nm, EUV dose = 14 mJ/cm^2 , CAR). The best exposure result is achieved for a mask-wafer distance of $324 \mu\text{m}$.

Compared to the designed elbow test structure (Fig. 2), the experiment indicates, that the best results are obtained for a distance between $314 \mu\text{m}$ and $334 \mu\text{m}$ as compared to the designed focal distance of $300 \mu\text{m}$. However, the lines are not continuous, and some gaps appear. For further inspections a focal distance of $324 \mu\text{m}$ is used as optimal focal distance. The best exposure results for all 16 elbow structures of different feature width (from 100 nm to 800 nm) and pitch size (from 200 nm to 1600 nm) are shown in Fig. 9. The smallest resolved feature width is $302 \text{ nm} \pm 27 \text{ nm}$.

In Fig. 10, the exposure results employing the optimized distance of mask and wafer are depicted. Here, exposures using the plasma-based laboratory source and synchrotron exposures are compared with the simulation of the intensity distribution at the wafer plane for the designed mask (pixels with intensity values above or below selected thresholds are colored white or black respectively, see color scale). Overall, the results from the synchrotron exposures look similar to those from the plasma-based source. At the synchrotron setup, the variation of the mask to wafer distance is limited by the employed hardware, therefore, the exposures are slightly out of focus and the resulting elbow structure shows more line breaks.

The different spatial coherence length of both sources did not affect the exposure results. The size of the mask including all 16 elbows counterpart structures is 1 mm^2 , hence, the coherence length of the plasma source ($l_{\text{plasma}} = 13.5 \mu\text{m}$) is smaller and that of the synchrotron ($l_{\text{synchrotron}} = 1.19 \text{ mm}$) is larger than the mask size. Consequently, using the plasma source the illumination of the mask is not fully coherent. However, in both cases elbow structures in wafer plane are created. This is expected in the proximity regime, where only structures from a small sub-region of the mask contribute to image formation at a certain point at wafer. Furthermore, in both exposure experiments not exposed pattern regions in the resist are obtained, demonstrating the desired small (below threshold) exposure dose, even though there are no areas on the mask that can lead to complete absorption.

For comparison, the ASPW method is used to simulate the expected exposure results at the designed mask-wafer distance of $300 \mu\text{m}$ and the experimentally obtained mask-wafer distance of $324 \mu\text{m}$. In the simulations, four different masks are used: each of the simulated masks considers

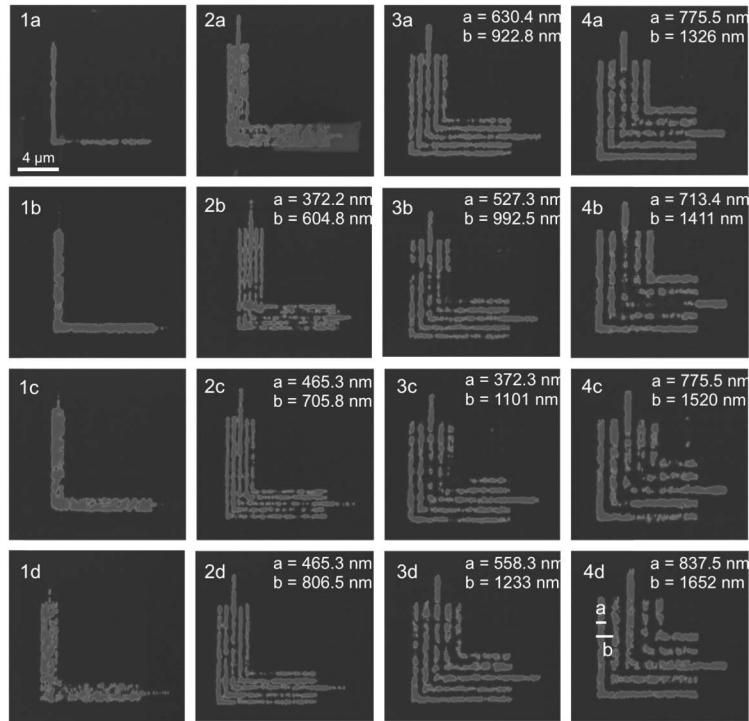


Fig. 9. The exposure result for the 16 elbow structures with plasma-based EUV source ($\lambda = 13.5$ nm, EUV dose = 14 mJ/cm^2 , CAR). The smallest resolved feature size is achieved for elbow structure 2b. Here, a is the pitch size, b corresponds to one period.

different aspects of the experimentally obtained mask (see Fig. 11). The first mask (Fig. 11(a)) is the initial simulated design of the holographic mask with only two phase levels (side view, no material or 330 nm phase shifting material). The top view of the mask is the simulated image with sharp edges and an exact square pixel size of $50 \times 50 \text{ nm}^2$. The simulated exposure results show the expected elbow structures and an even distribution of the intensity inside the elbow structures. The focal distance is as designed at $300 \mu\text{m}$. The second mask (Fig. 11(b)) uses an AFM-scan of the fabricated mask (Fig. 6 (b)) for the lateral dimensions of the mask (see top view), to take the more rounded shapes of the pixels of the fabricated mask into account. The mask side view remains still the same as for the previous mask with only two discrete phase levels. The simulations show more line breaks in the elbow structures and an uneven intensity distribution within the elbow pattern. The intensity at the ends of the longest line is higher than the intensity along the edges of the lines and around the corners of the lines. The focal distance broadens to a range between $300 \mu\text{m}$ to $324 \mu\text{m}$. The third mask (Fig. 11(c)) uses also the AFM-scan for the lateral dimensions of the mask structures. Additionally, the height information of the AFM-scan is used to take the not fully structured resist layer into account but at optimal total thickness. Therefore the height information is scaled so that the maximal thickness of the phase shifting material is still the designed 330 nm but without the two discrete phase levels. All different height levels and pixel shapes (Fig. 7) are taken into account. Compared to the exposure results of the second mask (Fig. 11(b)) even more line breaks appear and the intensity distribution is uneven but the focal distance stays the same. This simulated exposure result matches the experimentally obtained exposure result (see Fig. 10). The fourth mask (Fig. 11(d)) is the same as the third mask but the maximal thickness of the phase shifting material is set to 80 nm which equals to the fully

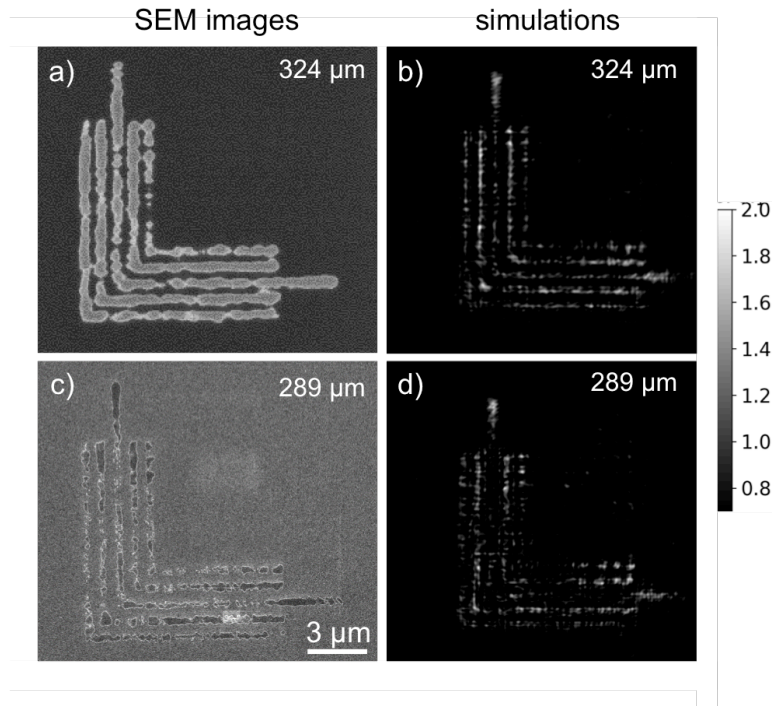


Fig. 10. Direct comparison between simulated (c, d) and exposure results with laboratory exposure tool (a) and at synchrotron setup (b) (SEM images, scale bar for all equals 3 μm). Plasma-based exposure: $\lambda = 13.5$ nm, EUV dose = 14 mJ/cm^2 , CAR. Synchrotron exposure: $\lambda = 13.5$ nm, EUV dose = 64.76 mJ/cm^2 , HSQ-based resist.

structured portion of the resist contributing to the phase-shift as seen in the FIB-cut (Fig. 7). This mask represents the closest match to the fabricated mask. The simulated exposure result only differs in intensity from the third exposure result as the intensity is overall lower but the intensity distribution is the same. This simulation is closest to the experimental exposure result. As conclusion, the focal distance of this mask is between 300 μm and 324 μm . This analysis indicates that the focal point is shifted due to the different pixel shapes and multiple phase levels of the fabricated mask and not due to the different thickness of the phase shifting layer.

The contrast of those simulated images is defined by the modulation transfer function $MTF = (I_{max} - I_{min}) / (I_{max} + I_{min})$ with I_{max} being the maximal intensity (threshold corresponding to the dose to clear) and I_{min} the minimal intensity (threshold for the onset dose) of the calculated intensity modulation in the simulation result. To determine these thresholds, minimal and maximal intensity of the color scale are varied in 0.1 steps until only the elbow structures are visible and all other additional structures disappear. Exposure results with additional features outside the elbow structure are defined as overexposed. The MTF is maximal for mask (b) in Fig. 11. Compared to masks (c) and (d) this is expected, since mask (b) has only two well-controlled phase levels and not multiple of those with different values as in mask (c) and (d). The MTF of mask (b) is higher than that of mask (a), but at the cost of a more uneven intensity distribution in the exposure result. The MTF thus depends not only on the thickness of the phase shifting material but also on the pixel shape.

The fabricated holographic mask was capable of producing the elbow structures on the substrates employing exposures at the plasma-based source as well as at the synchrotron. A feature width of $302 \text{ nm} \pm 27 \text{ nm}$ was realized. The main limitation for the minimal feature

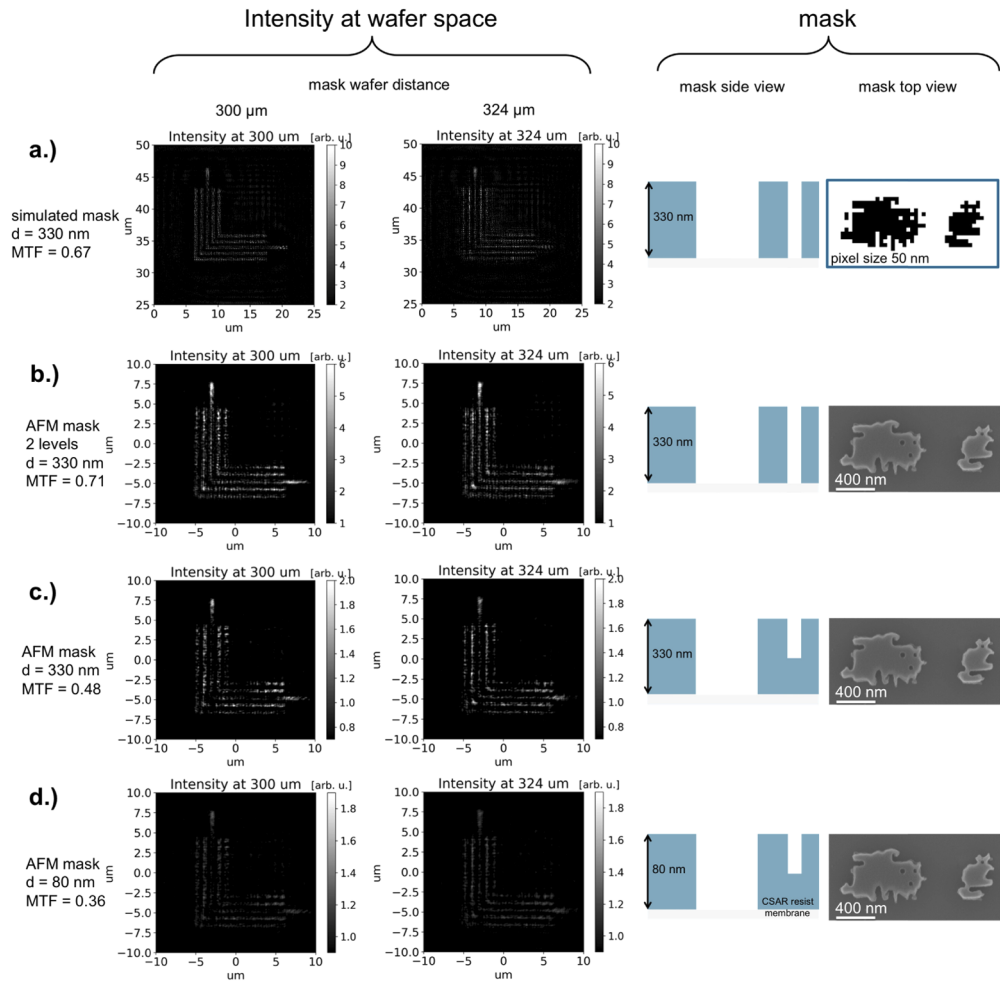


Fig. 11. Simulated exposure results of one elbow structure for the designed mask-wafer distance (300 μm) and the experimentally obtained focal distance (324 μm). Each simulation considers different holographic mask geometry, as shown in the side and top view images. Here d is the maximal thickness of the phase shifting layer, MTF - modulation transfer function of the resulting image.

size and smoothness of the printed resist structures is the mask fabrication process. The mask fabrication process limits the minimal pixel size due to high aspect ratio, which also influences the resist development. The resist development can be improved by utilizing a mega sonic bath during the development process to ensure that the developer reaches all areas. Further, the parameters of the electron beam writing process need investigation regarding short range correction and a smaller beam current to achieve better control of structures on the mask. The mask fabrication process can be improved in future work by using metal-based phase-shifting materials to reduce requirements on material thickness for a desired phase-shift, e.g. down to ~ 100 nm thickness for molybdenum or niobium [23]. Consequently, the pixel size can be reduced to $15 \times 15 \text{ nm}^2$ while maintaining the same aspect ratio, leading to an increase in the resolution of the generated image [24]. Further improvement of the printed structures will be achieved by introducing more than two phase-shifting levels on the mask (multilevel phase-shifting mask). This can be realized by utilizing gray scale lithography [25] or thermal scanning probe lithography [26]. Both approaches

allow for multilevel control of the remaining resist thickness at nanoscale patterning. Either this resist can be used directly as the phase shifting medium or the structures will be transferred via etching into another phase-shifting material.

A hologram can be described as a superposition of Fresnel zone plates and therefore the minimum feature size on the hologram mask determines the achievable resolution similar to the outer zone width of a Fresnel zone plate. Utilizing higher diffraction orders gives a possibility to improve the resolution even further [24]. Ultimately, the minimal resolution is improved by increasing the numerical aperture either by decreasing the mask-wafer distance or by increasing the area of the hologram contributing to the image formation via interference at the wafer plane and therefore by the coherence of the source [27]. Other than the mask fabrication issue we need to improve mask-wafer distance control. With such small depth of focus already a small deviation from the focus position influences the pattern fidelity negatively. However the discussed issues (mask fabrication, coherence requirements and the focus position control) are not more challenging to overcome than in projection lithography. From computational/algorithm side, compared with computational lithography at deep ultraviolet wavelength (193 nm), EUV has the advantage of an easier modeling process of the mask but is more challenging in modeling the resist response [28].

Overall, we conclude that the developed algorithms can be successfully applied to mask design in EUV spectral range. The mask manufacturing process has to be further optimized in order to obtain the desired printed patterns and to further increase the resolution of the model.

4. Summary and outlook

The principle of printing arbitrary structures into a resist by EUV radiation using a synthetically generated holographic mask is demonstrated. Printing elbow test patterns with EUV radiation at 13.5 nm wavelength was successfully realized both with synchrotron and plasma-based radiation. The differences of the fabricated elbow structures from the designed ones were successfully reproduced in the simulations, confirming the functionality of the developed algorithms. The reasons for the deviations of the fabricated pixel shapes from the designed ones can be attributed to shortcomings of processing, i.e. an underdevelopment of various resist structures. Further optimization of the relatively simple fabrication process of the mask will produce the desired aspect ratio of the holographic mask and will substantially improve the observed results. This can be done either by changing the exposure and development times or by employing other phase-shift materials with lower thickness. In general, we have demonstrated a feasible approach for an effective lens-less patterning method of arbitrary structures on the nanoscale.

Funding

Horizon 2020 Framework Programme (654360); Helmholtz Association (Helmholtz Professorship); Bundesministerium für Bildung und Forschung (13N14151).

Acknowledgements

Portions of this work were presented at the conference “SPIE Photomask Technology + EUV Lithography” in 2018, 108091A. This work was realized by cooperation activities within the frame of the Jülich Aachen Research Alliance for Fundamentals of Future Information Technology (JARA-FIT). Part of this work was performed at Helmholtz Nanoelectronic Facility of Forschungszentrum Jülich [29]. Special thanks to Stephan Trellenkamp for the help with the eBeam writing. Other parts of this work were performed at Paul Scherrer Institute Switzerland within the NFFA-Program. Special thanks to Dimitrios Kazazis and Michaela Vockenhuber for the help at the synchrotron.

Disclosures

Larissa Juschkin: KLA Corporation (E). Jan Biller and Maciej Grochowicz: ASML Veldhoven (E). The authors declare no conflicts of interest.

References

1. S. Brose, J. Tempeler, S. Danylyuk, P. Loosen, and L. Juschkin, "Achromatic Talbot lithography with partially coherent extreme ultraviolet radiation: process window analysis," *J. Micro/Nanolith. MEMS MOEMS* **15**(4), 043502 (2016).
2. S. Bühling, F. Wyrowski, E. B. Kley, A. J. M. Nellissen, L. Wang, and M. Dirkzwager, "Resolution enhanced proximity printing by phase and amplitude modulating masks," *J. Micromech. Microeng.* **11**(5), 603–611 (2001)..
3. T. Weichelt, U. Vogler, L. Stuerzebecher, R. Voelkel, and U. D. Zeitner, "Resolution enhancement for advanced mask aligner lithography using phase-shifting photomasks," *Opt. Express* **22**(13), 16310–16321 (2014)..
4. S. Danylyuk, H. Kim, S. Brose, C. Dittberner, P. Loosen, T. Taubner, K. Bergmann, and L. Juschkin, "Diffraction-assisted extreme ultraviolet proximity lithography for fabrication of nanophotonic arrays," *J. Vac. Sci. Technol., B: Nanotechnol. Microelectron.: Mater., Process., Meas., Phenom.* **31**(2), 021602 (2013)..
5. G. Kunkemöller, T. W. W. Maß, A.-K. U. Michel, H.-S. Kim, S. Brose, S. Danylyuk, T. Taubner, and L. Juschkin, "Extreme ultraviolet proximity lithography for fast, flexible and parallel fabrication of infrared antennas," *Opt. Express* **23**(20), 25487–25495 (2015)..
6. F. Wyrowski, E.-B. Kley, S. Bühling, A. J. M. Nellissen, L. Wang, and M. Dirkzwager, "Proximity printing by wave-optically designed masks," *Proc. SPIE* **4436**, 130–139 (2001).
7. R. W. Gerchberg and W. O. Saxton, "A practical algorithm for the determination of the phase from image and diffraction plane pictures," *Optik* **35**, 237–246 (1972).
8. D. G. Voelz, "Computational Fourier Optics: A MATLAB Tutorial," SPIE Tutor. Texts **TT89** (2011).
9. S. Danylyuk, P. Loosen, K. Bergmann, H. Kim, and L. Juschkin, "Scalability limits of Talbot lithography with plasma-based extreme ultraviolet sources," *J. Micro/Nanolith. MEMS MOEMS* **12**(3), 033002 (2013)..
10. C. Mack, "Impact of mask roughness on wafer line-edge roughness," *Proc. SPIE* **7488**, 748828 (2009)..
11. X. Ma and G. R. Arce, *Computational Lithography*, Wiley Seri (2011).
12. R. W. Wake and M. C. Flanagan, "A review of contrast in positive photoresists," *Proc. SPIE* **0539**, 291–298 (1985)..
13. M. J. Bowden, "Physics and Chemistry of the Lithographic Process," *J. Electrochem. Soc.* **128**(5), 195C (1981)..
14. Allresist GmbH Germany, "Positiv - E-Beam Resists AR-P 6200 (CSAR 62)," 20–29 (2017).
15. B. L. Henke, E. M. Gullikson, and J. C. Davis, "X-ray interactions: photoabsorption, scattering, transmission, and refelction at E=50-30000 eV, Z=1-92," *At. Data Nucl. Data Tables* **54**(2), 181–342 (1993)..
16. J. Kirz, "Phase zone plates for x rays and the extreme uv," *J. Opt. Soc. Am.* **64**(3), 301 (1974)..
17. H. W. Schnopper, L. P. Van Speybroeck, J. P. Delvaille, A. Epstein, E. Killne, R. Z. Bachrach, J. Dijkstra, and L. Lantward, "Diffraction grating transmission efficiencies for XUV and soft x rays," *Appl. Opt.* **16**(4), 1088–1091 (1977)..
18. S. Brose, S. Danylyuk, L. Bahrenberg, R. Lebert, P. Loosen, and L. Juschkin, "Optimized phase-shifting masks for high-resolution resist patterning by interference lithography," *Proc. SPIE* **10450**, 104502A (2017).
19. V. Deuter, M. Grochowicz, J. Biller, S. Brose, S. Danylyuk, T. Taubner, D. Grützmacher, and L. Juschkin, "Holographic masks for computational proximity lithography with EUV radiation," *Proc. SPIE* **10809**, 108091A (2018).
20. S. Brose, S. Danylyuk, L. Bahrenberg, R. Lebert, J. Stollenwerk, P. Loosen, and L. Juschkin, "EUV-LET 2.0: a compact exposure tool for industrial research at a wavelength of 13.5 nm," *Proc. SPIE* **10957**, 109571K (2019).
21. SLS - Swiss Light Source, Paul Scherrer Institut, Forschungsstr. 111, 5232 Villigen, Switzerland.
22. S. Brose, S. Danylyuk, J. Tempeler, H.-S. Kim, P. Loosen, and L. Juschkin, "Enabling laboratory EUV research with a compact exposure tool," *Proc. SPIE* **9776**, 97760R (2016)..
23. B. Lüttgenau, S. Brose, S. Danylyuk, J. Stollenwerk, and P. Loosen, "Novel high-contrast phase-shifting masks for EUV interference lithography," *Proc. SPIE* **11323**, 113231Q (2020).
24. Y. C. Cheng, A. Isoyan, J. Wallace, M. Khan, and F. Cerrina, "Extreme ultraviolet holographic lithography: Initial results," *Appl. Phys. Lett.* **90**(2), 023116 (2007)..
25. J. Kim, D. C. Joy, and S.-Y. Lee, "Controlling resist thickness and etch depth for fabrication of 3D structures in electron-beam grayscale lithography," *Microelectron. Eng.* **84**(12), 2859–2864 (2007)..
26. H. Wolf, C. Rawlings, P. Mensch, J. L. Hedrick, D. J. Coady, U. Duerig, and A. W. Knoll, "Sub-20 nm silicon patterning and metal lift-off using thermal scanning probe lithography," *J. Vac. Sci. Technol., B: Nanotechnol. Microelectron.: Mater., Process., Meas., Phenom.* **33**(2), 02B102 (2015).
27. A. Isoyan, Y. C. Cheng, F. Jiang, J. Wallace, F. Cerrina, and S. Bollepalli, "Progress in extreme ultraviolet interferometric and holographic lithography," *J. Vac. Sci. Technol., B: Nanotechnol. Microelectron.: Mater., Process., Meas., Phenom.* **25**(6), 2145–2150 (2007)..
28. A. Erdmann, T. Fühner, F. Shao, and P. Evanschitzky, "Lithography Simulation: Modeling Techniques and Selected Applications," *Proc. SPIE* **7390**, 739002 (2009)..
29. W. Albrecht, J. Moers, and B. Hermanns, "HNF - Helmholtz Nano Facility," *J. large-scale Res. Facil. JLSRF* **3**, 1–9 (2017).